Direct Polariton-To-Electron Tunneling in Quantum Cascade Detectors Operating in the Strong Light-Matter Coupling Regime

M. Lagrée,[1,*] M. Jeannin,[2,§] G. Quinchard,[1,§] O. Ouznali,[2] A. Evirgen,[1] V. Trinité,[1,†]
R. Colombelli,[2,‡] and A. Delga[1]

[1] *III-V Lab, Campus Polytechnique, 1, Avenue Augustin Fresnel, RD 128, Palaiseau cedex 91767, France*
[2] *Centre de Nanosciences et de Nanotechnologies (C2N), CNRS UMR, 9001, Université Paris-Saclay, Palaiseau 91120, France*

(Received 27 October 2021; revised 11 March 2022; accepted 28 March 2022; published 12 April 2022)

Modern optoelectronic devices rely on cavity electrodynamics concepts for improved performances, embedding the active medium in an optical cavity to enhance the light-matter coupling. This coupling rate is usually small compared to the electronic and photon energies. Despite several demonstrations, devices operating with much larger light-matter coupling strength, in the so-called strong light-matter coupling regime, are yet to be demonstrated as viable, practical candidates. One of the main technological obstacles that hamper their dissemination is the comprehension of the carrier current extraction and injection from and into strongly coupled light-matter states. Here, we study this fundamental phenomenon in midinfrared quantum cascade detectors (QCDs) operating in the moderate to strong light-matter coupling regime. They operate around $\lambda = 10$ μm with a minimum Rabi splitting of 9.3 meV. A simple model based on the usual description of transport in QCDs does not reproduce the polaritonic features in the photocurrent spectra. On the contrary, a more refined approach, based on the semiclassical coupled modes theory, is capable of reproducing both optical and electrical spectra with excellent agreement. By correlating absorption and photoresponse with the simulations, we demonstrate that—in this system—resonant tunneling from the polaritonic states appears to be the predominant extraction mechanism. The dark intersubband states do not have a significant role in the process, contrary to what happens in electrically injected polaritonic emitters.

DOI: 10.1103/PhysRevApplied.17.044021

I. INTRODUCTION

Polaritons, hybrid light-matter quasiparticles that arise when an electromagnetic field is strongly coupled to a matter (electronic) excitation, are an ideal playground to explore interesting physical phenomena and applications. Their matter part can be any polarization-carrying excitation, among which phonons [1], excitons [2], molecular vibrations [3], cyclotron transitions [4], or intersubband (ISB) transitions [5,6]. Despite the large variety of polariton families, they share a common characteristic that motivates the continuous research in polariton physics: the light-matter coupling rate Ω can redefine the dominant energy or time scale in the system over those of the uncoupled constituents. Hence, they have been used as versatile platforms to test various fundamental phenomena [7] such as Bose-Einstein condensation [8], topological effects [9], ultrastrong coupling [4,10], or the modification of energy landscapes in chemical reactions [11]. Simultaneously to the constant progress in understanding polariton physics, they are pushed towards applications, with, e.g., midinfrared (MIR) optical polaritonic devices [12,13] or as an alternative degree of freedom to alter the transport characteristics of electronic systems [14–16].

One of the most widespread application targets across the diverse polariton communities is the polaritonic emitter, producing coherent radiation with a higher efficiency than its counterpart operating in the weak light-matter coupling regime (e.g., light-emitting devices or lasers). Coherent, laserlike emission from microcavity exciton polaritons condensates has been demonstrated in the visible part of the electromagnetic spectrum [17], while coherent midinfrared thermal emitters have been realized [18–20] for applications that do not require laser light. Efforts are ongoing to develop MIR and THz lasers based on ISB polaritons [21], arising from the strong light-matter coupling between an ISB transition and a photonic microcavity mode, as they are predicted to have improved functionalities with respect to current technology [22,23].

---

[*] mathurin.lagree@3-5lab.fr
[†] virginie.trinite@3-5lab.fr
[‡] raffaele.colombelli@u-psud.fr
[§] These authors contributed equally.

However, efficient electrical injection into polaritonic devices is a major challenge, with few experimental demonstrations present in the literature [24,25]. The reason is that most of the electrons injected from an electronic reservoir into a polaritonic system tunnel into dark states [22,26]. These states do not couple to the electromagnetic field [22] and do not contribute to the emission process. The impossibility to experimentally achieve elevated efficiencies of these strongly coupled devices is the main motivation of the present work.

To circumvent the injection problem and to get insightful information on the transport mechanisms between electronic and polaritonic states, the authors of Ref. [27] studied the reverse phenomenon: the extraction of an electrical current from a polaritonic reservoir, i.e., a detection process. Indeed, previous reports of photodetection in the strong coupling regime [28,29] brought little information on the electronic extraction process. The work in Ref. [27] demonstrated photocurrent extraction from microcavity polaritons into the continuum of electronic states using quantum-well photodetectors and proposed an empirical model of the current extraction. Although this is a step towards a better understanding of polaritonic devices, in the perspective of developing efficient light-emitting devices, there is a strong need to study the *resonant* current extraction from a polaritonic state into an electronic state, as well as to clarify the impact of dark states in the extraction process. Quantum cascade detectors (QCDs) [30–32], photovoltaic counterparts of quantum-well photodetectors, rely on the resonant extraction of electrons into a cascade of discrete energy levels, and thus are perfectly suitable to further elucidate the problem.

In this context, we investigate MIR QCDs ($\lambda = 10\ \mu$m) embedded in patch microcavities, operating at the onset of the strong light-matter coupling regime ($2\Omega_{\text{Rabi}} = 9.3$ meV). We observe the characteristic spectral features of this regime on both reflectivity and photocurrent measurements. Using a semiclassical model based on the coupled-mode theory (CMT) and by explicitly incorporating the spectral properties of the extraction cascade, we are able to reproduce quantitatively both reflectivity and photoresponse spectra.

From this analysis, we can conclude that there is a direct resonant tunneling process between the polaritonic states and the electronic extractor state, and that dark states are not involved. It is therefore possible to circumvent the problem of dark states when extracting an electrical current from a polaritonic reservoir.

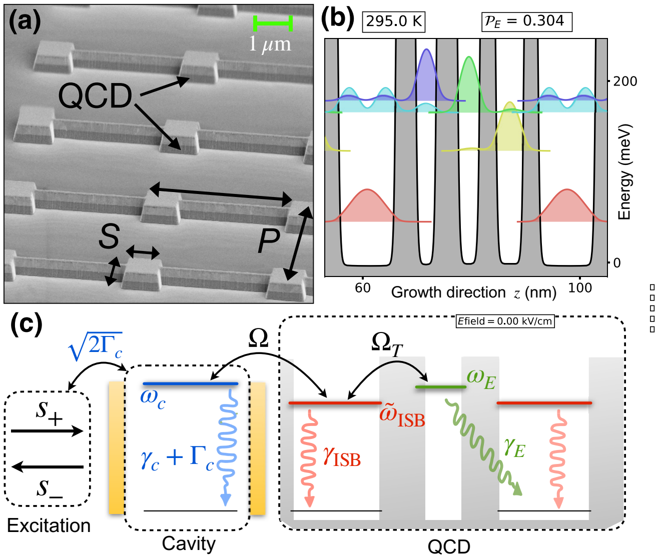

FIG. 1. (a) SEM image of a patch cavity-embedded QCD detector. S is the patch lateral size and P is the array period. Patches are electrically connected using gold wires deposited on a dielectric bridge layer. The active layers, the QCDs, are embedded between gold layers (Au). (b) Band structure of the QCD [**11.0**/3.6/**4.2**/3.8/**4.6**/2.8/**5.3**/2.5 nm, starting with the doped quantum well $n_{2\text{D}} = 5e11\ \text{cm}^{-2}$, (In, Ga)As in bold, (Al, In)As normal], represented on one period ($T = 295$K). (c) Schematic representation of the system: the incoming light excitation (ω) couples to the optical cavity (ω_c), which is coupled to the intersubband transition ($\tilde{\omega}_{\text{ISB}}$). The ISB mode is itself coupled to an extractor mode (ω_E), representing the electronic cascade. The different dissipation channels are represented (γ_c, Γ_c, γ_{ISB}, and γ_E).

II. DEVICE DESIGN AND PASSIVE CHARACTERIZATIONS

A. Fabrication and measurements

We first investigate the optical properties of patch antenna arrays embedding the QCD active region. The metal-metal patch resonators are obtained through wafer-bonding on a metallized Si substrate. They are processed into 1×2 mm^2 matrices of period P and patch dimensions S with different (P, S) values [Fig. 1(a)]. Changing the period P allows to optimize the optical coupling into the cavities, while the patch size S tunes the resonance frequency. The active layers are grown by molecular beam epitaxy (MBE). They form a five-period (In, Ga)As/(Al, In)As QCD detector, surrounded by 50-nm, n-doped (Si, $n_{3\text{D}} = 6 \times 10^{17}$ cm^{-3}) (In, Ga)As contacts. The active quantum wells, where the intersubband absorption takes place, are n-doped (Si, $n_{2\text{D}} = 5 \times 10^{11}$ cm^{-2}). The QCD band structure [Fig. 1(b)] is designed using a numerical software (METIS) relying on a refined and self-consistent Schrödinger-Poisson scheme [33,34]. Computations account for electron wave-vector dispersion, nonparabolicity effects as well as coherent tunneling. The electronic subbands are aligned such that undesirable diagonal transitions between levels (resulting in dark current leakages) are minimized, while photocurrent extraction is maximized through the optimization of the cascade alignment and barrier thickness. We compute a 0.3 extraction probability $\mathcal{P}_E$ at 295 K. A conceptual representation of the whole structure is displayed on Fig. 1(c).

Two samples are processed for reflectivity measurements: a sample with undoped active layers inside the patch resonators (the empty cavity set) and a sample with the Si-doped quantum wells. In this experiment, the patch antennas are not electrically connected by wires. The measurements are carried out using a Fourier-transform infrared spectrometer (FTIR, Bruker Vertex 70) using a pair of parabolic ($F = 180$ mm) and elliptic mirrors ($F = 282/42$ mm) and a deuterated triglycine sulfate detector MIR detector. The reflectivity of the sample is normalized by the reflectivity spectrum of an Au mirror reference. All the measurements are performed at 295 K with a 13° incidence angle and the light is p polarized. For both samples (doped and undoped), the reflectivity $\mathcal{R}$ is measured for different couples (P, S) of patch dimensions.

We show in Fig. 2 the experimental absorption $\mathcal{A} = 1 - \mathcal{R}$ determined from the array reflectivity $\mathcal{R}$ (continuous lines) for the undoped sample [Fig. 2(a)] or the doped sample [Fig. 2(b)]. The undoped sample exhibits a single absorption peak corresponding to the cavity mode only, that blue shifts in frequency for decreasing patch size S. The doped sample exhibits two resonances for each cavity size, which anticross around $\omega \approx 120$ meV for a cavity size $S \approx 1.55$ μm. A minimal splitting of approximately equal to 9 meV is estimated: this characteristic anticrossing around the ISB transition energy is a signature of the strong coupling regime. We detail below a quantitative assessment of the polaritonic features in the absorption spectra.

B. Two-resonator coupled-mode theory

To model the optical response of the system, we use a semiclassical formalism, the coupled-mode theory. It describes in a phenomenological way the coupling between resonators and the dissipative interaction with their environment [36,37]. The CMT is a straightforward and powerful formalism that has been repeatedly used in the literature to successfully describe the optical response of intersubband devices embedded in metal-insulator-metal (M-I-M) resonators [6,13,27,38,39]. Both of the ISB plasmonic mode and electromagnetic cavity mode are represented as coupled harmonic oscillators. The generic equation describing the evolution of the modes amplitude **a** interacting with one excitation port is [40–43]

$$\frac{d\mathbf{a}}{dt} = [i\mathcal{H} - (\boldsymbol{\gamma} + \boldsymbol{\Gamma})]\,\mathbf{a} + K s_{+} e^{i\omega t}, \qquad (1)$$

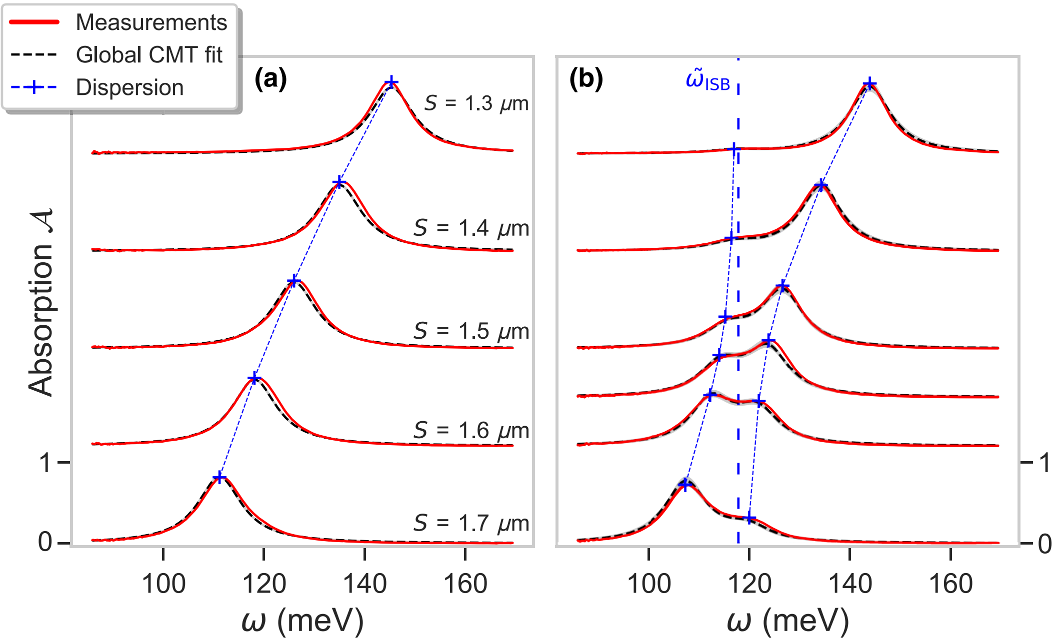

FIG. 2. Reflectivity measurements (continuous lines) and CMT global fit (dashed lines), represented in the form of absorption $\mathcal{A} = 1 - \mathcal{R}$, for different patch sizes S and fixed period $P = 5$ μm. The scale used is the same for all spectra and offsets are added for visibility. (a) Empty cavities (undoped active layers). Cavity dispersion (blue crosses) is computed using Eq. (3) ($n_{\rm eff} = 3.28$) (b) Doped QCDs ($n_{2\rm D} = 5e11$ cm^{-2}) embedded inside the patch cavities. Polaritonic dispersion is computed using the Hamiltonian $\mathcal{H}$ in Eq. (2) ($n_{\rm eff} = 3.33$, $\omega_{\rm ISB} = 115$ meV, $\omega_P = 25$ meV). See Fig. S1 within the Supplemental Material [35] for additional reflectivity measurements and fits. Although extremely low, propagated errors from the fit are represented on the spectra with the thickness of the gray curves.

with

$$\mathcal{H} = \begin{bmatrix} \omega_c & \Omega \\ \Omega & \tilde{\omega}_{\mathrm{ISB}} \end{bmatrix}, \; \boldsymbol{\gamma} + \boldsymbol{\Gamma} = \begin{bmatrix} \gamma_c + \Gamma_c & 0 \\ 0 & \gamma_{\mathrm{ISB}} \end{bmatrix},$$
$$\mathbf{a} = \begin{bmatrix} a_c \\ a_{\mathrm{ISB}} \end{bmatrix}, \; K = \begin{bmatrix} \sqrt{2\Gamma_c} \\ 0 \end{bmatrix}. \tag{2}$$

The hermitian Hamiltonian $\mathcal{H}$ describes the unitary evolution of the system, $\boldsymbol{\Gamma}$ the dissipative interaction with the impinging light excitation (i.e., the radiative coupling), $\boldsymbol{\gamma}$ the dissipative interaction with all the other external modes and K the coupling between the system and the excitation. $|s_+|^2$ is the power of the impinging light excitation and $|a_i|^2$ is the energy stored in the i resonator. The rotating-wave approximation is applied, meaning that any contribution from antiresonant modes ($-\omega_c$ and $-\tilde{\omega}_{\mathrm{ISB}}$) is neglected and that the system is restricted to two resonators.

The first resonator is the optical cavity, modeling the TM_{01} electromagnetic mode confined in the patch antennas. The dispersion relation of the mode is directly related to the lateral size S of the cavity [44]:

$$\omega_c = \frac{\pi c_0}{n_{\mathrm{eff}} S}. \tag{3}$$

The cavity frequency is thus entirely parameterized by S and n_{eff}, the effective index of the cavity, which represents the effective medium composed of the semiconductor contacts and the undoped periodic structure embedded between the gold layers. γ_c describes the mode losses, which include all possible decay channels within the cavity (free-carrier losses and interaction with phonons mainly).

The second resonator models the intersubband absorption. The plasma-shifted energy $\tilde{\omega}_{\mathrm{ISB}}$ is the renormalized eigenenergy of the ISB transition ω_{ISB}, considering electron-electron interaction through the plasma energy ω_P [5]:

$$\tilde{\omega}_{\mathrm{ISB}}^2 = \omega_{\mathrm{ISB}}^2 + \omega_P^2. \tag{4}$$

Note that this two-resonator CMT model implies that the ISB transition is homogeneously broadened, effectively assuming similar parabolic dispersion for both subbands. γ_{ISB} describes the intersubband losses, mainly due to the LO phonon scattering, interface roughness, and alloy disorder. The cavity and intersubband resonators are coupled through the light-matter coupling constant Ω [5]:

$$\Omega = \frac{\omega_P}{2}\sqrt{f_w}, \tag{5}$$

with f_w (≈ 0.17) the overlap factor between the cavity field and the doped active quantum wells. Since we expect an experimental deviation on the doping, we use the plasma energy ω_P as a fitting parameter, in order to compute both ISB eigenenergy $\tilde{\omega}_{\mathrm{ISB}}$ and light-matter coupling Ω. The Rabi splitting is defined as twice the coupling 2Ω and corresponds to the minimal splitting between the polaritonic branches.

Incident light couples to the system through the cavity radiative losses Γ_c. The patch array can be assimilated to a two-dimensional (2D) array of radiating slits, whose radiated power can be computed from interferometric considerations [45]. It allows parametrization of the radiative dissipative term Γ_c as follows, with the coefficient α_c:

$$\Gamma_c = \frac{\alpha_c}{P^2}, \tag{6}$$

with P the array period [Fig. 1(a)]. Adjusting P allows, in principle, to reach the patch cavity critical coupling ($\gamma_c = \Gamma_c$) where all incident energy is dissipated in the system.

The ISB mode does not couple directly to the incident light, it does so *via* the cavity mode: therefore, the ISB radiative coupling Γ_{ISB} is such that $\Gamma_{\mathrm{ISB}} \ll \Gamma_c$. However, before fully neglecting the direct radiative coupling of the ISB mode, we have to consider also the cross terms $\sqrt{\Gamma_{\mathrm{ISB}}\Gamma_c}$ describing the radiative coupling of the modes with each other via the excitation channel [42,46], as they can have considerable effects on the lineshapes in certain cases. At our doping levels [47], the condition $\Gamma_{\mathrm{ISB}}\Gamma_c \ll \Omega^2$ is verified, so Γ_{ISB} is indeed neglected.

In forced oscillation mode, the system of Eq. (1) is solved and the total absorption $\mathcal{A}$ is obtained considering the power dissipated through nonradiative processes inside the two resonators:

$$\mathcal{A} = \mathcal{A}_c + \mathcal{A}_{\mathrm{ISB}} = 2\gamma_c\frac{|a_c|^2}{|s_+|^2} + 2\gamma_{\mathrm{ISB}}\frac{|a_{\mathrm{ISB}}|^2}{|s_+|^2}, \tag{7}$$

where $\mathcal{A}_c$ and $\mathcal{A}_{\mathrm{ISB}}$ are the cavity and ISB contributions to absorption. The absorption of the undoped sample (empty cavities) is computed using Eqs. (1) and (7), removing the coupling to the ISB mode ($\Omega = 0$). It leads to the usual analytical expression of a Lorentzian absorption:

$$\mathcal{A}_{\text{empty cavity}} = \frac{4\gamma_c\Gamma_c}{(\Gamma_c + \gamma_c)^2 + (\omega - \omega_c)^2}. \tag{8}$$

Total absorption for the doped samples are computed using Eq. (7) and numerically fitted to the experimental data [48]. A global fit is performed using a unique set of parameters for the whole dataset formed by each couple (P, S), such that our problem is constrained to the maximal extent: the fitting parameters are $(n_{\mathrm{eff}}, \gamma_c, \alpha_c)$ for the empty cavities, $(n_{\mathrm{eff}}, \gamma_c, \alpha_c, \omega_{\mathrm{ISB}}, \omega_P, \gamma_{\mathrm{ISB}})$ for the doped samples. Results are presented in Fig. 2 (dashed black lines). See Fig. S1 within the Supplemental Material [35] for additional measurements on different (P, S) couples.

For both undoped [Fig. 2(a)] and doped [Fig. 2(b)] samples, we obtain an excellent agreement between the

TABLE I. Parameters returned by global CMT fits of the following: (a) reflectivity of the undoped samples [Eq. (8), $T = 300$ K]; (b) reflectivity of the doped samples [Eq. (7), $T = 300$ K]; (c) photocurrent of doped samples, electrically connected [Eq. (14), $T = 78$ K].

	(a) Reflectivity fit: bare cavity	(b) Reflectivity fit: $n_{2D} = 5e11$ cm^{-2}	(c) Photocurrent fit: $n_{2D} = 5e11$ cm^{-2}
n_{eff}	3.283 ± 0.001	3.333 ± 0.001	3.219 ± 0.001
γ_c (meV)	3.8 ± 0.1	3.5 ± 0.01	3.4 ± 0.01
α_c (meV μm^2)	38.5 ± 0.1	38.6 ± 0.1	29.1 ± 1.2
ω_{ISB} (meV)	–	115.0 ± 0.1	115.1 ± 0.1
γ_{ISB} (meV)	–	5.2 ± 0.1	3.3 ± 0.1
ω_P (meV)	–	25.6 ± 0.1	29.2 ± 0.1
ω_E (meV)	–	–	125.2 ± 0.1
γ_E (meV)	–	–	11.5 ± 0.1
Ω_T (meV)	–	–	3.7 ± 0.1

experimental data and the fit for the whole (P, S) dataset. Both cavity dispersion Eq. (3) and P dependency of the cavity broadening Eq. (6) are recovered. All along the anticrossing, the amplitudes of the polaritonic branches are well reproduced.

Fit parameters are summarized in Table I. Cavity parameters n_{eff}, γ_c, and α_c are coherent between the doped and undoped samples. We obtain a plasma frequency of 26 meV, which converts into a $2\Omega = 9.3$ meV Rabi splitting, according to Eq. (4). Polaritonic broadenings are estimated to be $\gamma_c + \Gamma_c + \gamma_{\text{ISB}}/2 \approx 5$ meV. Although we are only at the onset of the strong coupling regime, we are able to distinguish the two polaritonic contributions to the absorption spectra and estimate the Rabi splitting. The equivalent doping can therefore be computed using the plasma frequency expression:

$$\omega_P^2 = \frac{e^2 \Delta n_{1\to 2} f_{1\to 2}}{\epsilon\epsilon_0 m^* L_{\text{eff}}} \approx \frac{e^2 n_{2D} f_{1\to 2}}{\epsilon\epsilon_0 m^* L_{\text{QW}}}, \tag{9}$$

where $\Delta n_{1\to 2}$ is the electronic surface-density difference between the lower and upper subbands of the optical quantum well, $f_{1\to 2}$ is the oscillator strength of the ISB transition (= 0.84, computed using METIS), m^* is the effective electron mass, and L_{eff} is an effective length corresponding to the spatial extension of the ISB currents, that can be usually approximated by L_{QW}. We also neglect the electronic density thermally promoted to the excited state. We find a $n_{2D} = 3.7e11$ cm^{-2} equivalent doping, 35% lower than the expected one. The ISB energy is estimated around $\omega_{\text{ISB}} = 115$ meV, even though it is designed to be 120 meV. This experimental redshift is the consequence of the nonparabolicity of the subbands, unaccounted for in the CMT. It can be computed using the METIS software: at 300 K, we find that the absorption peak is indeed redshifted toward 116 meV.

Polaritonic dispersion is computed via the diagonalization of the Hamiltonian $\mathcal{H}$ of Eq. (2) and superimposed on the spectra [blue dotted lines Fig. 2(b)]. The absorption peaks closely follow the dispersion and $\tilde{\omega}_{\text{ISB}}$ is indeed an asympotic value of the polaritonic branches. The fit parameters present little correlation between one another, which propagates into low errors on the spectra (see Sec. I within the Supplemental Material [35] for the detailed computations of the errors). The weak experimental and theoretical disagreements are rather related to our oversimplified model and to the experimental dispersion (experimental uncertainties on S, P, n_{2D}, ω_{ISB} mainly).

III. PHOTOCURRENT MEASUREMENTS AND COMPARISON WITH MODELING

A. Measurements

We are now interested in the photodetection response of the devices operating in strong coupling. A set of smaller, 8×8 (approximately equal to 50×50 μm^2) patch antenna arrays is processed. In this experiment, patches are connected through 250-nm thin metallic wires realized by electron-beam lithography [Fig. 1(a)]. The samples are placed inside a cryostat ($T = 78$K) at zero voltage applied bias. [It is necessary to operate in such experimental conditions: as a matter of fact, we observe that the application of a (small) bias leads to a drastic decrease in the SNR that hampers the photocurrent measurement]. Samples are illuminated by the FTIR globar source, and the signal is acquired in rapid scan mode. Light is p polarized perpendicular to the wires, in order to excite the mode that is not perturbed by the wires [49]. The generated photocurrent is amplified using a low-noise transimpedance amplifier.

Measurements on devices with $P = 7$ μm are displayed in Fig. 3 (continuous lines), and all the photocurrent spectra are normalized to unity. See Fig. S2 within the Supplemental Material [35] for additional photocurrent measurements on devices with different (P, S) values. The photocurrent spectra exhibit two anticrossing peaks, the spectral signature of the strong light-matter coupling regime. Far from perfect anticrossing, the relative amplitude of these peaks appears to follow the opposite trend than the reflectivity measurements: for small S the peak located at the lower energy (contribution of the lower polaritonic mode) has a larger amplitude than the peak located at higher energy (contribution of the upper

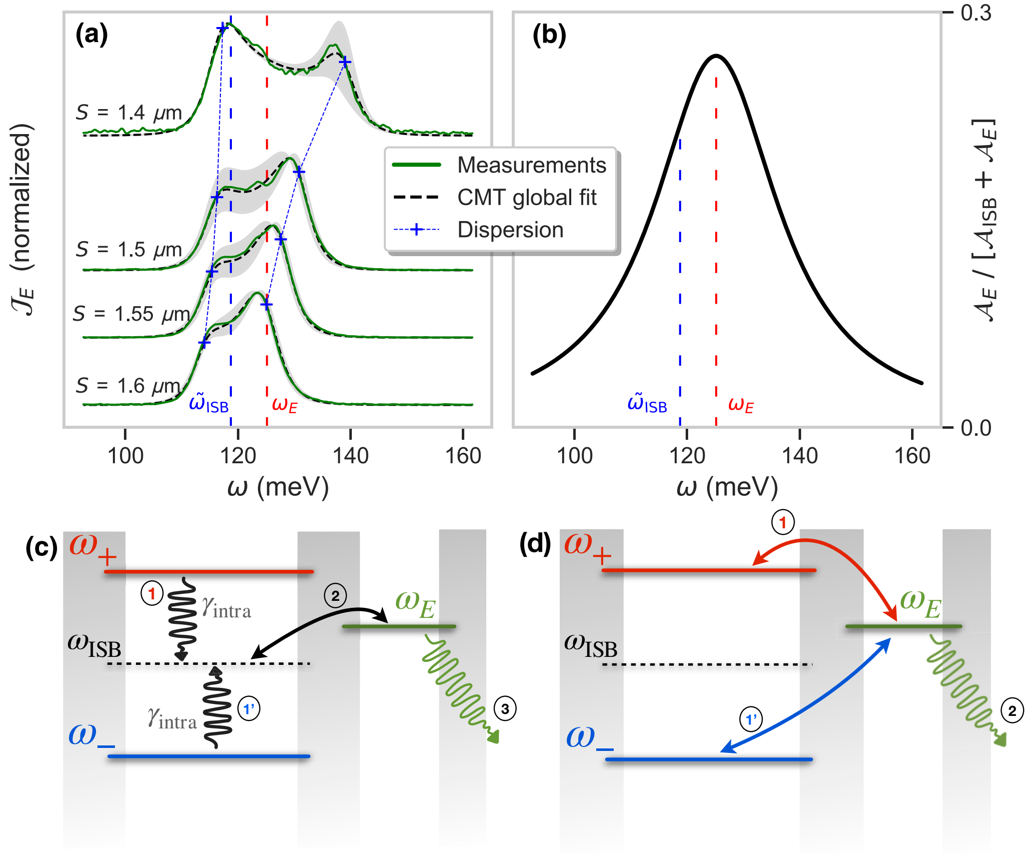

FIG. 3. (a) Normalized photocurrent measurements (continuous lines) and three-resonator CMT global fit (dashed lines), for devices with period $P = 7$ μm and different patch sizes S. Offsets are added for visibility. The gray areas represent the fit errors propagated on the spectra (see Sec. I within the Supplemental Material [35] for the detailed computations of the errors). The polaritonic dispersion (blue crosses) is computed considering only the cavity-ISB interaction in the Hamiltonian $\mathcal{H}$ of Eq. (11), unperturbed by the QCD extractor ($n_{\rm eff} = 3.23$, $\omega_{\rm ISB} = 115$ meV, $\omega_P = 29$ meV). (b) Computed transfer function between the extracted power ($\mathcal{A}_E$) and the total power dissipated inside the QCD ($\mathcal{A}_E + \mathcal{A}_{\rm ISB}$). Lower panels: possible extraction schemes for a QCD in the strong light-matter coupling regime. (c) Dark-state mediated extraction: polaritonic excitations ($\omega_\pm$) relax into the dark states ($\omega_{\rm ISB}$), and they are subsequently extracted through the electronic cascade. (d) Resonant tunneling through the polaritonic states: polaritonic excitations directly tunnel from the polaritonic reservoir into the electronic cascade. In this case the dark states are not involved in the process.

polaritonic mode), and this trend is reversed for high S. This is not surprising: we expect that the contribution of each polaritonic mode to the photocurrent mirrors the ISB mode proportion inside each one of the two modes. Far from resonance, the polaritonic mode closest to the ISB transition will be mainly matterlike, and will thus have a high relative peak amplitude in the photocurrent spectra, whereas the other polaritonic mode, mainly photonic, will have a smaller contribution.

However, the photocurrent spectra exhibit an additional unexpected feature. Equal peak amplitudes would be expected at the minimal polaritonic splitting $\omega_c = \tilde{\omega}_{\rm ISB}$, where both ISB and cavity fractions inside each mode are equal. This is not what we observe: equal peak amplitudes occur between $S = 1.5$ μm and $S = 1.4$ μm, at a different frequency $\omega \approx 125$ meV, although the minimal splitting is indeed located around $\tilde{\omega}_{\rm ISB}$ (around $S = 1.6$ μm) from the reflectivity measurements. This discrepancy is a crucial point: motivated by this observation, in the follow up we infer useful information on the electronic transport in this strongly coupled system.

Note, although the detector samples stem from the same wafer as the ones used for reflectivity measurements in Sec. II (the active region is the same), they are not identical. They are fabricated separately, and the patch cavities are not connected by wires in the samples used for reflectivity. For this reason, we cannot make a direct one-to-one comparison between samples with the same nominal parameters.

B. Modeling strategy

In the following section, we attempt to model and reproduce these photocurrent spectra, and we show that their peculiar features permit the extraction of information on the tunneling process between the polaritonic and electronic reservoirs in this system.

We develop and apply two different photocurrent models for QCDs operating in the strong light-matter coupling regime. The two approaches rely on different assumptions and model two different possible extraction schemes, as displayed in Figs. 3(c) and 3(d).

In the first scheme (c), photoexcited polaritons *first* decay into dark states, and then are extracted into the electronic reservoir, i.e., the QCD extractor. This is essentially the reverse of the process that has traditionally hampered polaritonic emitters [22,24,26].

The second scheme (d), on the other hand, does not involve the dark states: polaritons directly tunnel into the electronic reservoir. Our goal is to understand if the experimental results can discriminate between the two processes and tell us which extraction scheme is at work in the studied devices.

C. Dark-state mediated extraction: two-resonator CMT

In the weak light-matter coupling regime, the usual description of transport inside quantum cascade detectors and ISB devices, in general, relies on the hypothesis that intrasubband processes (γ_{intra}, scattering *inside* the subbands) are significantly faster than intersubband processes [50,51], and are responsible for the subband thermalization. This allows a Markovian and sequential vision of transport: after an intersubband hop, electrons are first thermalized inside the subband before the next hop, following the Fermi-Dirac distribution. Memory of the previous hop is lost, and hops are independent. The subbands in this picture are simple electronic reservoirs exchanging excitations. Electronic transport is treated with perturbation theory and semiclassical rate equations [33,52,53]. Although a strong tunnel coupling Ω_T betweeen two electronic subbands can create coherent Rabi oscillations between the two subbands, the strong dephasing effects of the intrasubband dynamics ensure the sequential treatment of the transport from one band to another [54,55]. In this framework, the photocurrent $\mathcal{J}_E$ (at zero bias) is proportional to the ISB absorption [32]:

$$\mathcal{J}_E(\omega) \propto \mathcal{P}_E \mathcal{A}_{\mathrm{ISB}}(\omega). \tag{10}$$

The scalar transfer function $\mathcal{P}_E$ is the extraction probability, i.e., the probability that an electron promoted to the excited state of the ISB transition escapes to the ground state of the next adjacent period, through the extraction cascade. In the weak excitation regime, $\mathcal{P}_E$ is independent of the impinging light frequency ω: the memory of an initial photoelectron generation into the excited state of the ISB transition (a ω-dependant process) is erased by the fast intrasubband decoherence. All the subsequent hopping of the electronic excitation to other subbands will thus occur at rates independent of the excitation frequency ω. In this scenario, the generated photocurrent has the same spectral shape as the ISB contribution to the absorption.

We are interested in extending this standard description of transport in QCDs to the strong light-matter coupling regime. A simplified representation of the system is displayed in Fig. 3(c). The strong light-matter coupling Ω between the bright ISB mode and the cavity mode give rise to the polaritonic eigenmodes $\omega_\pm$. Impinging light of frequency ω can be tuned to generate polaritonic excitations in either $\omega_\pm$ modes. However, in a sequential treatment of the extraction, we expect the intrasubband dynamic γ_{intra} to erase the polaritonic nature of the photoexcitation prior to any extraction mechanism into the electronic cascade. In other words, due to the predominant intrasubband decoherence, the optically pumped polaritons *first* collapse into the ISB dark modes ω_{ISB}, *then* they are extracted—as electronic excitations—through the cascade, as they would be in a QCD operating in the weak coupling regime. As previously, such a sequential process implies a scalar transfer function, independent of the light frequency ω: a similar spectral shape for the ISB absorption $\mathcal{A}_{\mathrm{ISB}}(\omega)$ and the photocurrent $\mathcal{J}_E$ is expected in this scenario.

This dark-state mediated extraction scheme can be faithfully modeled by the two-resonator CMT model developed in Eq. (2). The *normalized* photocurrent experimental spectra can indeed be fitted using only the *normalized* ISB component $\mathcal{A}_{\mathrm{ISB}}$ of the total absorption Eq. (7), because they are expected to have a similar spectral shape. We perform a global fit of the photocurrent measurements using n_{eff}, γ_c, α_c, ω_{ISB}, ω_P, γ_{ISB} as parameters. The fit results are presented in Fig. S3 within the Supplemental Material [35].

The general quality of the fit is poor: the spectral linewidths and the peak positions are not well reproduced. In particular, the peculiar features of the photocurrent around the cavity-ISB resonance are misrepresented: equal peak amplitudes of the polaritonic branches are predicted for $S \approx 1.6$ μm, whereas the experiments clearly reveal this condition at $S \approx 1.45$ μm. As a consequence, the $S = 1.5, 1.55$, and 1.6 μm spectra are poorly reproduced. We emphasize that the dissociation between the minimal splitting and the equal peak amplitudes is a key feature of these measurements. The impossibility to properly reproduce this dissociation suggests that modeling the photocurrent through the use of the ISB part of the total absorption $\mathcal{A}_{\mathrm{ISB}}$ only, i.e., using a frequency-independent transfer function $\mathcal{P}_E$, is not sufficient. This is equivalent to saying that the dark-state mediated extraction, schematically represented in Fig. 3(c), is probably not the process that enables operation of the QCDs in the strong light-matter coupling regime.

D. Resonant extraction: three-resonator CMT

We therefore develop a second photocurrent model that explicitly describes the extraction process and is able to model a resonant extraction mechanism, as sketched in Fig. 3(d).

To this scope, we introduce an additional mode in the CMT model, the extraction mode ω_E. It effectively models the electronic cascade. A schematic representation of the CMT implementation of the complete system—i.e., optical cavity, ISB transition, and extraction—is displayed in Fig. 1(c). The extraction mode is coupled to the ISB mode through a tunnel coupling constant Ω_T, and it dissipates electrons into the next period at a rate γ_E. Obviously, it cannot directly couple to the incident light ($\Gamma_E = 0$). Equation (2) is modified introducing a third resonator of amplitude a_E:

$$\mathcal{H} = \begin{bmatrix} \omega_c & \Omega & 0 \\ \Omega & \tilde{\omega}_{\mathrm{ISB}} & \Omega_T \\ 0 & \Omega_T & \omega_E \end{bmatrix}, \ \boldsymbol{\gamma} + \boldsymbol{\Gamma} = \begin{bmatrix} \gamma_c + \Gamma_c & 0 & 0 \\ 0 & \gamma_{\mathrm{ISB}} & 0 \\ 0 & 0 & \gamma_E \end{bmatrix},$$

$$\mathbf{a} = \begin{bmatrix} a_c \\ a_{\mathrm{ISB}} \\ a_E \end{bmatrix}, \ K = \begin{bmatrix} \sqrt{2\Gamma_c} \\ 0 \\ 0 \end{bmatrix}. \tag{11}$$

The system total absorption $\mathcal{A}$ is the sum of the power dissipated into the different decay channels, normalized by the incoming power $|s_+|^2$:

$$\mathcal{A}_{\mathrm{tot}} = \mathcal{A}_c + \mathcal{A}_{\mathrm{ISB}} + \mathcal{A}_E \tag{12}$$

$$= 2\gamma_c \frac{|a_c|^2}{|s_+|^2} + 2\gamma_{\mathrm{ISB}} \frac{|a_{\mathrm{ISB}}|^2}{|s_+|^2} + 2\gamma_E \frac{|a_E|^2}{|s_+|^2}. \tag{13}$$

The net photocurrent $\mathcal{J}_E$ is defined as the current under illumination subtracted from the dark current. Since the measurements are performed at zero bias, there is no dark current and the photocurrent $\mathcal{J}_E$ is proportional to the power dissipated from a period to the next adjacent period. This is exactly the power dissipated by the additional extraction mode:

$$\mathcal{J}_E \propto 2\gamma_E |a_E|^2. \tag{14}$$

In this theoretical framework, the transfer function between the photocurrent and the total power dissipated inside the QCD is no longer independent of the impinging light frequency ω. It is instead defined as $T(\omega)$, and can be analytically computed:

$$T(\omega) = \frac{\mathcal{A}_E}{\mathcal{A}_{\mathrm{ISB}} + \mathcal{A}_E} \tag{15}$$

$$= \frac{\gamma_E}{\gamma_{\mathrm{ISB}}} \frac{\Omega_T^2}{(\omega - \omega_E)^2 + \gamma_E^2 + \frac{\gamma_E}{\gamma_{\mathrm{ISB}}} \Omega_T^2}. \tag{16}$$

Explicitly writing $T(\omega)$ reveals that it is a Lorentzian function that peaks at ω_E with a width given by the extractor dissipation rate γ_E and tunnel coupling rate Ω_T [Fig. 3(b)].

Note, $T(\omega)$ is independent of the cavity parameters and of the light-matter coupling constant Ω: it is therefore the same for all (S, P) samples. A frequency-dependent transfer function was used previously in the literature. Vigneron *et al.* [27] introduced it to model the transport mechanisms underlying the tunnel coupling process in a quantum well infrared photodetector detector. Earlier, Sapienza *et al.* [24] introduced a phenomenological Gaussian transfer function between the electroluminescence and the absorption spectra. In this work, the Lorentzian transfer function directly arises from the model and it is not introduced as a phenomenological parameter.

To test the model against the experiments, we perform a global fit of the experimental photocurrent spectra, using Eq. (14) with the following fit parameters: n_{eff}, γ_c, α_c, ω_{ISB}, ω_P, γ_{ISB}, ω_E, γ_E, Ω_T. The photocurrent curves arising from the modeling are represented in Fig. 3(a) as dashed lines for devices with $P = 7$ μm. See Fig. S2 within the Supplemental Material [35] for additional (P, S) couples. We obtain an excellent agreement between the experimental and computed spectra: we are now able to reproduce both peak positions and linewidths. Crucially, the three-resonator CMT reproduces the features that the two-resonator CMT of Sec. III C is unable to predict: minimal splitting and equal polaritonic peak amplitudes occurring at different S for absorption versus photocurrent. This is a direct consequence of the peaked spectral shape of the transfer function $T(\omega)$ of Eq. (15), which modifies the polaritonic peak amplitudes without introducing a substantial spectral shift.

Note, the energy where the upper and lower polaritonic modes contribute equally to the photocurrent is significantly higher than in the absorption spectra (cf. Fig. 2). The absorption magnitude closely follows the cavity proportion of the two polaritons, while this direct link between Hopfield coefficients and relative peak amplitude of the spectra does not hold for the photocurrent. See Fig. S4 within the Supplemental Material [35] for a direct graphical evidence of this observation, with a careful comparison between cavity-ISB weights and peak amplitudes.

The fitted parameters are reported in Table I(c). They are extremely consistent with the parameters returned by the reflectivity fit. The small variations observed between photocurrent and reflectivity parameters are attributed to different measuring temperatures (lower losses γ_c and γ_{ISB}, in particular, for lower temperature) and the different technological processes between the two experiments. The extraction mode energy ω_E is estimated to be about 125 meV, which is coherent with the predicted alignment between the upper optical level and extraction level, designed such that $\omega_E - \omega_{\mathrm{ISB}} = 10$ meV [Fig. 1(b)]. The tunnel coupling $\Omega_T = 3.5$ meV is also equal to the value computed using our numerical software (METIS). Finally, the extraction rate γ_E is estimated around 11 meV, significantly faster than the other dissipation rates γ_{ISB} and

γ_c, which is consistent with the idea that the cascade is an efficient extractor.

E. Physical interpretation of the modeling results

The ability of the three-resonator CMT model to correctly reproduce the peculiar features of the photocurrent spectra validates the process sketched in Fig. 3(d): polaritons are extracted into the electronic reservoir *via* a resonant process that does not involve the dark states. It is useful to detail a few subtleties of the model.

Being a semiclassical formalism, CMT is only able to describe dissipative processes: damping dissipates both modes' populations $|a_i|^2$ and coherences $a_i^* a_j$. The model is, however, unable to depict pure decoherence effects, i.e., processes that affect only coherences, without dissipating the modes' populations. Specifically in our system, the CMT is unable to describe the intrasubband dynamics of transport γ_{intra}, as it does not affect the subbands' populations, erasing only the coherence between them (through thermalization). The underlying hypothesis of this CMT model is therefore that the intrasubband processes are significantly slower than any other transport mechanisms and thus are neglected. In particular, it describes accurately situations where $\gamma_{\text{intra}} \ll \Omega_T$. Memory of the polaritonic nature of the excitation is carried out during the extraction.

The CMT and the sequential transport models are valid in two precise limiting cases. The former one applies if the intrasubband dynamics γ_{intra} is neglected with respect to the tunnel coupling extraction Ω_T ($\gamma_{\text{intra}} \ll \Omega_T$). The latter one applies instead if the intrasubband dynamics dominates the tunnel extraction ($\gamma_{\text{intra}} \gg \Omega_T$). These asymptotic behaviors are mirrored by the frequency dependency of the transfer function: a sharp $T(\omega)$ in the case of the CMT, a flat probability for the sequential model.

A rigorous treatment of the problem based on the density matrix formalism [56] is currently being developed to investigate the regimes in which either limiting models (CMT and sequential transport) are valid, and to provide a bridge between the two. We expect to recover the asymptotic behavior of both CMT and sequential models by tuning the γ_{intra} parameter with respect to the Ω_T parameter.

Nevertheless, the three-resonator CMT model correctly describes the extraction scheme represented in Fig. 3(d): the polaritons are directly extracted from the polaritonic states into the electronic cascade, without any involvement of the dark ISB modes in the process.

The three-resonator formulation of the CMT therefore provides a compact and convenient model for a complicated system in a nonstandard operating regime. It provides an intuitive representation of the system, and also a robust framework to analyse and interpret the experimental data. In particular, the excellent agreement it provides between experiment and computed photocurrent measurements, permits the elucidation of the nature of the polariton-to-electron transport in these strongly coupled devices. It appears that the transport between the polaritonic states and the electronic extraction state is not dominated by the intrasubband decoherence, but rather by a delocalized transport induced by the coherent couplings Ω and Ω_T.

IV. CONCLUSION

We demonstrate quantum cascade detectors embedded in patch antenna resonators operating in the moderate to strong light-matter coupling regime ($2\Omega_R = 9.3$ meV). By correlating reflectivity and photoresponse measurements, we elucidate the process of resonant tunnel extraction of ISB microcavity polaritons into an electronic reservoir. The comparison with a specifically developed three-resonator CMT model allows us to understand crucial details of the polaritonic transport. We show that—in this system—resonant tunneling from the polaritonic states appears to be the predominant extraction mechanism: most of the polaritonic excitations are directly extracted into the electronic cascade before they collapse into the dark states due to decoherent intrasubband scattering. The dark ISB states do not have a significant role in the process, contrary to what happens in electrically injected polaritonic emitters.

This work also strengthens the use of quantum cascade detectors as key devices to study ISB polaritons. The first natural follow up of this work is the exploration of a wider range of ISB-cavity coupling rates. Higher doping is required ($n_{2D} \approx 10^{12}$ cm^{-2}). On the theoretical side, it would be useful to explicitly incorporate the intrasubband dynamics γ_{intra} using the density matrix formalism [56–58]. Finally, the demonstration that it is possible to engineer a resonant tunneling extraction of polaritons into an electronic reservoir, without involvement of the dark states, paves the way toward a better understanding of polaritonic transport, with the ultimate goal of implementing efficient electrical injection in polaritonic light-emitting devices [23,24,59].

ACKNOWLEDGMENTS

We acknowledge S. Barbieri, J-F. Lampin, and M. Hakl of the *Institut d'Electronique, de Microélectronique et de Nanotechnologie* (IEMN) for the electromagnetic simulation and design of the patch antenna arrays.

We acknowledge financial support from the French National Research Agency: project SOLID (ANR-19-CE24-0003-02), HISPANID (ANR-17-ASTR-0008-01), and IRENA (ANR-17-CE24-0016).

We acknowledge financial support from the European Union FET-Open Grant MIR-BOSE (No. 737017).

[1] S. Foteinopoulou, G. C. R. Devarapu, G. S. Subramania, S. Krishna, and D. Wasserman, Phonon-polaritonics: Enabling powerful capabilities for infrared photonics, Nanophotonics **8**, 2129 (2019).

[2] C. Weisbuch, M. Nishioka, A. Ishikawa, and Y. Arakawa, Observation of the Coupled Exciton-Photon Mode Splitting in a Semiconductor Quantum Microcavity, Phys. Rev. Lett. **69**, 3314 (1992).

[3] A. Shalabney, J. George, J. Hutchison, G. Pupillo, C. Genet, and T. W. Ebbesen, Coherent coupling of molecular resonators with a microcavity mode, Nat. Commun. **6**, 5981 (2015).

[4] G. Scalari, C. Maissen, D. Turcinkova, D. Hagenmuller, S. De Liberato, C. Ciuti, C. Reichl, D. Schuh, W. Wegscheider, M. Beck, and J. Faist, Ultrastrong coupling of the cyclotron transition of a 2D electron gas to a THz metamaterial, Science **335**, 1323 (2012).

[5] Y. Todorov and C. Sirtori, Intersubband polaritons in the electrical dipole gauge, Phys. Rev. B **85**, 045304 (2012).

[6] J.-M. Manceau, S. Zanotto, T. Ongarello, L. Sorba, A. Tredicucci, G. Biasiol, and R. Colombelli, Mid-infrared intersubband polaritons in dispersive metal-insulator-metal resonators, Appl. Phys. Lett. **105**, 081105 (2014).

[7] I. Carusotto and C. Ciuti, Quantum fluids of light, Rev. Mod. Phys. **85**, 299 (2013).

[8] J. Kasprzak, M. Richard, S. Kundermann, A. Baas, P. Jeambrun, J. M. J. Keeling, F. M. Marchetti, M. H. Szymańska, R. André, J. L. Staehli, V. Savona, P. B. Littlewood, B. Deveaud, and L. S. Dang, Bose–Einstein condensation of exciton polaritons, Nature **443**, 409 (2006).

[9] T. Jacqmin, I. Carusotto, I. Sagnes, M. Abbarchi, D. D. Solnyshkov, G. Malpuech, E. Galopin, A. Lemaître, J. Bloch, and A. Amo, Direct Observation of Dirac Cones and a Flatband in a Honeycomb Lattice for Polaritons, Phys. Rev. Lett. **112**, 116402 (2014).

[10] T. Laurent, Y. Todorov, A. Vasanelli, A. Delteil, C. Sirtori, I. Sagnes, and G. Beaudoin, Superradiant Emission from a Collective Excitation in a Semiconductor, Phys. Rev. Lett. **115**, 187402 (2015).

[11] M. Hertzog, M. Wang, J. Mony, and K. Börjesson, Strong light–matter interactions: A new direction within chemistry, Chem. Soc. Rev. **48**, 937 (2019).

[12] S. Pirotta, N.-L. Tran, A. Jollivet, G. Biasiol, P. Crozat, J.-M. Manceau, A. Bousseksou, and R. Colombelli, Fast amplitude modulation up to 1.5 GHz of mid-IR free-space beams at room-temperature, Nat. Commun. **12**, 799 (2021).

[13] M. Jeannin, J.-M. Manceau, and R. Colombelli, Unified Description of Saturation and Bistability of Intersubband Transitions in the Weak and Strong Light-Matter Coupling Regimes, Phys. Rev. Lett. **127**, 187401 (2021).

[14] E. Orgiu, J. George, J. A. Hutchison, E. Devaux, J. F. Dayen, B. Doudin, F. Stellacci, C. Genet, J. Schachenmayer, C. Genes, G. Pupillo, P. Samorì, and T. W. Ebbesen, Conductivity in organic semiconductors hybridized with the vacuum field, Nat. Mater. **14**, 1123 (2015).

[15] C. Naudet-Baulieu, N. Bartolo, G. Orso, and C. Ciuti, Dark vertical conductance of cavity-embedded semiconductor heterostructures, New J. Phys. **21**, 093061 (2019).

[16] F. Appugliese, J. Enkner, G. L. Paravicini-Bagliani, M. Beck, C. Reichl, W. Wegscheider, G. Scalari, C. Ciuti, and J. Faist, Breakdown of topological protection by cavity vacuum fields in the integer quantum Hall effect, Science **375**, 1030 (2022).

[17] M. D. Fraser, S. Höfling, and Y. Yamamoto, Physics and applications of exciton–polariton lasers, Nat. Mater. **15**, 1049 (2016).

[18] J.-J. Greffet, R. Carminati, K. Joulain, J.-P. Mulet, S. Mainguy, and Y. Chen, Coherent emission of light by thermal sources, Nature **416**, 61 (2002).

[19] M. De Zoysa, T. Asano, K. Mochizuki, A. Oskooi, T. Inoue, and S. Noda, Conversion of broadband to narrowband thermal emission through energy recycling, Nat. Photonics **6**, 535 (2012).

[20] G. Lu, J. R. Nolen, T. G. Folland, M. J. Tadjer, D. G. Walker, and J. D. Caldwell, Narrowband polaritonic thermal emitters driven by waste heat, ACS Omega **5**, 10900 (2020).

[21] C. Ciuti, G. Bastard, and I. Carusotto, Quantum vacuum properties of the intersubband cavity polariton field, Phys. Rev. B **72**, 115303 (2005).

[22] S. De Liberato and C. Ciuti, Quantum model of microcavity intersubband electroluminescent devices, Phys. Rev. B **77**, 155321 (2008).

[23] R. Colombelli and J.-M. Manceau, Perspectives for Intersubband Polariton Lasers, Phys. Rev. X **5**, 011031 (2015).

[24] L. Sapienza, A. Vasanelli, R. Colombelli, C. Ciuti, Y. Chassagneux, C. Manquest, U. Gennser, and C. Sirtori, Electrically Injected Cavity Polaritons, Phys. Rev. Lett. **100**, 136806 (2008).

[25] P. Jouy, A. Vasanelli, Y. Todorov, L. Sapienza, R. Colombelli, U. Gennser, and C. Sirtori, Intersubband electroluminescent devices operating in the strong-coupling regime, Phys. Rev. B **82**, 045322 (2010).

[26] S. De Liberato and C. Ciuti, Quantum theory of electron tunneling into intersubband cavity polariton states, Phys. Rev. B **79**, 075317 (2009).

[27] P.-B. Vigneron, S. Pirotta, I. Carusotto, N.-L. Tran, G. Biasiol, J.-M. Manceau, A. Bousseksou, and R. Colombelli, Quantum well infrared photo-detectors operating in the strong light-matter coupling regime, Appl. Phys. Lett. **114**, 131104 (2019).

[28] E. Dupont, H. C. Liu, A. J. SpringThorpe, W. Lai, and M. Extavour, Vacuum-field Rabi splitting in quantum-well infrared photodetectors, Phys. Rev. B **68**, 245320 (2003).

[29] L. Sapienza, A. Vasanelli, C. Ciuti, C. Manquest, C. Sirtori, R. Colombelli, and U. Gennser, Photovoltaic probe of cavity polaritons in a quantum cascade structure, Appl. Phys. Lett. **90**, 201101 (2007).

[30] L. Gendron, M. Carras, A. Huynh, V. Ortiz, C. Koeniguer, and V. Berger, Quantum cascade photodetector, Appl. Phys. Lett. **85**, 2824 (2004).

[31] B. Schwarz, P. Reininger, A. Harrer, D. MacFarland, H. Detz, A. M. Andrews, W. Schrenk, and G. Strasser, The limit of quantum cascade detectors: A single period device, Appl. Phys. Lett. **111**, 061107 (2017).

[32] A. Delga, Quantum cascade detectors: A review, Mid-infrared Optoelectronics, 337 (2020).

[33] V. Trinité, E. Ouerghemmi, V. Guériaux, M. Carras, A. Nedelcu, E. Costard, and J. Nagle, Modelling of electronic

transport in quantum well infrared photodetectors, Infrared Phys. Technol. **54**, 204 (2011).

[34] R. L. Terazzi, *Transport in quantum cascade lasers*, Ph.D. thesis, ETH Zurich (2012).

[35] See Supplemental Material at http://link.aps.org/supplemental/10.1103/PhysRevApplied.17.044021 for additional reflectivity measurements and fits in Fig. S1, the detailed computations of the propagated errors in Sec. I, additional photocurrent measurements on devices with different geometries in Fig. S2, results of the photocurrent fits using a two resonators coupled-mode-theory model in Fig. S3, and comparison between cavity-ISB weights and peak amplitudes in Fig. S4.

[36] S. Miller, Coupled wave theory and waveguide applications, Bell System Tech. J. **33**, 661 (1954).

[37] H. Haus, Waves and fields in optoelectronics., PRENTICE-HALL, INC., ENGLEWOOD CLIFFS, NJ 07632, USA, 1984, 402, 197 (1984).

[38] J. Manceau, G. Biasiol, N. Tran, I. Carusotto, and R. Colombelli, Immunity of intersubband polaritons to inhomogeneous broadening, Phys. Rev. B **96**, 235301 (2017).

[39] M. Jeannin, T. Bonazzi, D. Gacemi, A. Vasanelli, L. Li, A. G. Davies, E. Linfield, C. Sirtori, and Y. Todorov, Absorption engineering in an ultrasubwavelength quantum system, Nano Lett. **20**, 4430 (2020).

[40] S. Zanotto, F. P. Mezzapesa, F. Bianco, G. Biasiol, L. Baldacci, M. S. Vitiello, L. Sorba, R. Colombelli, and A. Tredicucci, Perfect energy-feeding into strongly coupled systems and interferometric control of polariton absorption, Nat. Phys. **10**, 830 (2014).

[41] S. Fan, W. Suh, and J. D. Joannopoulos, Temporal coupled-mode theory for the fano resonance in optical resonators, JOSA A **20**, 569 (2003).

[42] W. Suh, Z. Wang, and S. Fan, Temporal coupled-mode theory and the presence of non-orthogonal modes in lossless multimode cavities, IEEE J. Quantum Electron. **40**, 1511 (2004).

[43] Z. Zhao, C. Guo, and S. Fan, Connection of temporal coupled-mode-theory formalisms for a resonant optical system and its time-reversal conjugate, Phys. Rev. A **99**, 033839 (2019).

[44] Y. Todorov, L. Tosetto, J. Teissier, A. M. Andrews, P. Klang, R. Colombelli, I. Sagnes, G. Strasser, and C. Sirtori, Optical properties of metal-dielectric-metal microcavities in the thz frequency range, Opt. Express **18**, 13886 (2010).

[45] C. A. Balanis, *Antenna Theory: Analysis and Design* (John wiley & sons, Hoboken, New Jersey, USA, 2016).

[46] F. Le Kien and A. Rauschenbeutel, Nanofiber-mediated chiral radiative coupling between two atoms, Phys. Rev. A **95**, 023838 (2017).

[47] C. Ciuti and I. Carusotto, Input-output theory of cavities in the ultrastrong coupling regime: The case of time-independent cavity parameters, Phys. Rev. A **74**, 033811 (2006).

[48] M. Newville, *et al.*, lmfit/lmfit-py 1.0.2 (2021).

[49] M. Hakl, Q. Lin, S. Lepillet, M. Billet, J.-F. Lampin, S. Pirotta, R. Colombelli, W. Wan, J. C. Cao, H. Li, E. Peytavit, and S. Barbieri, Ultrafast quantum-well photodetectors operating at 10 micron with a flat frequency response up to 70 ghz at room temperature, ACS Photonics **8**, 464 (2021).

[50] C. Koeniguer, G. Dubois, A. Gomez, and V. Berger, Electronic transport in quantum cascade structures at equilibrium, Phys. Rev. B **74**, 235325 (2006).

[51] A. Buffaz, A. Gomez, M. Carras, L. Doyennette, and V. Berger, Role of subband occupancy on electronic transport in quantum cascade detectors, Phys. Rev. B **81**, 075304 (2010).

[52] A. Delga, M. Carras, V. Trinité, V. Guériaux, L. Doyennette, A. Nedelcu, H. Schneider, and V. Berger, Master equation approach of classical noise in intersubband detectors, Phys. Rev. B **85**, 245414 (2012).

[53] S. Saha and J. Kumar, Rate equation modelling and investigation of quantum cascade detector characteristics, Superlattices Microstruct. **98**, 70 (2016).

[54] R. Kazarinov and R. Suris, Electric and electromagnetic properties of semiconductors with a superlattice, Soviet Phys. Semicond.-USSR **6**, 120 (1972).

[55] H. Willenberg, G. Döhler, and J. Faist, Intersubband gain in a bloch oscillator and quantum cascade laser, Phys. Rev. B **67**, 085315 (2003).

[56] M. Schlosshauer, Quantum decoherence, Phys. Rep. **831**, 15 (2019).

[57] H.-P. Breuer and F. Petruccione, *et al.*, *The Theory of Open Quantum Systems* (Oxford University Press on Demand, 2002).

[58] E. del Valle Reboul, *Quantum electrodynamics with quantum dots in microcavities*, Ph.D. thesis, Universidad Autónoma de Madrid (2008).

[59] R. Colombelli, C. Ciuti, Y. Chassagneux, and C. Sirtori, Quantum cascade intersubband polariton light emitters, Semicond. Sci. Technol. **20**, 985 (2005).